Improved stability and efficiency of CdSe/Sb<sub>2</sub>Se<sub>3</sub> thin-film solar cellsLiping Guo<sup>a</sup>, Corey Grice<sup>b</sup>, Baiyu Zhang<sup>c</sup>, Scott Xing<sup>d</sup>, Lin Li<sup>a</sup>, Xiaofeng Qian<sup>c</sup>, Feng Yan<sup>a,e,\*</sup><sup>a</sup> Department of Metallurgical and Materials Engineering, The University of Alabama, Tuscaloosa, AL 35487, USA<sup>b</sup> Department of Physics and Astronomy, and Wright Center for Photovoltaics Innovation and Commercialization, University of Toledo, Toledo, OH 43606, USA<sup>c</sup> Department of Materials Science and Engineering, Texas A&M University, College Station, TX 77843, USA<sup>d</sup> United Microelect Corp. Ltd., 3 Pasir Ris Dr. 12, Singapore 519528, Singapore<sup>e</sup> Center for Materials for Information Technology, The University of Alabama, Tuscaloosa, AL 35487, USA

## ARTICLE INFO

## Keywords:

Sb<sub>2</sub>Se<sub>3</sub> thin-film solar cell  
Close space sublimation  
CdSe window layer  
Stability  
Diffusion

## ABSTRACT

Quasi-one-dimensional van der Waals Sb<sub>2</sub>Se<sub>3</sub> compound is a promising absorber material with desired optical properties and has theoretical potential to achieve high power conversion efficiency (PCE) of ~30%. Here, we report a new window layer, *i.e.*, sputtered CdSe, which can enhance the Sb<sub>2</sub>Se<sub>3</sub> device stability during light soaking and improve the photocurrent collection. Compared to the widely used CdS window layer, CdSe can suppress the interfacial diffusion between the window layer and the Sb<sub>2</sub>Se<sub>3</sub> film, thereby reducing interfacial recombination sites. The dominant degradation mechanism in the CdS/Sb<sub>2</sub>Se<sub>3</sub> devices is found to be the S diffusion instead of the Cd diffusion, as CdSe/Sb<sub>2</sub>Se<sub>3</sub> devices did not show degradation during the 85 °C 120 h 1-Sun light soaking with similar Cd diffusion. Meanwhile, the enhanced photocurrent and reduced series resistivity in the CdSe/Sb<sub>2</sub>Se<sub>3</sub> solar cells lead to an improved PCE of 4.5% with a glass/FTO/CdSe/Sb<sub>2</sub>Se<sub>3</sub>/graphite cell architecture. The obtained results suggest that CdSe can be employed as a window layer in the thin-film solar cells made of stable and efficient Sb<sub>2</sub>Se<sub>3</sub>-like quasi-one-dimensional van der Waals materials, providing a cost-effective way to integrate into the traditional thin-film solar cell manufacturing process.

## 1. Introduction

Environmentally benign, stable, and cost-effective thin-film solar cells are highly desirable for producing affordable and sustainable renewable energy (Sivaram and Kann, 2016). Recently, perovskite solar cells (PVSC), CdTe and CuInGaSe based thin-film solar cells have achieved record PCE of more than 22%, approaching the theoretical Shockley-Queisser limit (~30%) (Green and Bremner, 2016; Polman et al., 2016). However, the stability issue of organic components in PVSC, a limited reserve of Te, and the high cost of Ga/In remain the bottlenecks for these thin-film solar cells to extend the market share dominated by the traditional Si module (Bosio et al., 2018; Rajagopal et al., 2018). Recently, antimony chalcogenide (*i.e.*, Sb<sub>2</sub>Se<sub>3</sub>) thin film solar cells have attracted a lot of interest as Sb<sub>2</sub>Se<sub>3</sub> is cost-effective solar absorber material with low-toxicity and affordable cost (Chen et al., 2018; Deng et al., 2018; Hu et al., 2018a; Razykov et al., 2018; Wang et al., 2017a, 2019; Zhang et al., 2018). Its suitable bandgap (*e.g.*, Sb<sub>2</sub>Se<sub>3</sub> ~1.1 eV) and high absorption coefficient (~10<sup>5</sup> cm<sup>-1</sup>) are similar to the highly successful Si and CuInGaSe (CIGS) commercial solar cells (Hutter et al., 2018; Kondrotas et al., 2019; Li et al., 2019; Liu et al., 2015, 2017; Zhao et al., 2018). Additionally, its non-cubic

orthorhombic crystal structure provides carrier transport along the intrinsic quasi-one-dimensional (Sb<sub>4</sub>Se<sub>6</sub>)<sub>n</sub> ribbons and possesses benign grain boundaries due to the weak van der Waals (vdWs) boundary, which could help prevent the grain boundaries issues as often observed in the cubic CdTe cells where, for example, boundary passivation is often required (Chen et al., 2018; Guo et al., 2018; Li et al., 2018a; Liang et al., 2018; Shongalova et al., 2018).

However, the structural difference between the orthorhombic Sb<sub>2</sub>Se<sub>3</sub> and the general cubic thin film solar cells, such as cubic CdTe technology, poses challenges to the growth of high-quality Sb<sub>2</sub>Se<sub>3</sub> absorber. The device performance is significantly influenced by the orientation of the (Sb<sub>4</sub>Se<sub>6</sub>)<sub>n</sub> ribbons in bulk Sb<sub>2</sub>Se<sub>3</sub>. For instance, the (1 2 0)-orientation film has a higher resistivity than that of the (2 1 1) and (2 2 1)-orientated film (Chen et al., 2018; Liu et al., 2014; Ngo et al., 2014). Thus, to improve the Sb<sub>2</sub>Se<sub>3</sub> device performance, it is critical to control the growth conditions, such as substrate temperature (Steinmann et al., 2015). Highly efficient Sb<sub>2</sub>Se<sub>3</sub> solar cells have been fabricated by rapid thermal evaporation (RTE), (Wang et al., 2017a) close space sublimation (CSS), (Li et al., 2018a) sputtering, (Liang et al., 2018; Shongalova et al., 2018) and vapor transport deposition (VTD) (Hu et al., 2018b; Khan et al., 2018; Yuan et al., 2016) by controlling

\* Corresponding author.

E-mail address: [fyan@eng.ua.edu](mailto:fyan@eng.ua.edu) (F. Yan).<https://doi.org/10.1016/j.solener.2019.06.042>

Received 27 January 2019; Received in revised form 13 June 2019; Accepted 17 June 2019

0038-092X/ © 2019 Published by Elsevier Ltd on behalf of International Solar Energy Society.

the substrate and source temperature to tailor the film texture. Meanwhile, various window layers for  $\text{Sb}_2\text{Se}_3$  cells, such as  $\text{CdS}$ ,  $\text{ZnO}$ ,  $\text{ZnMgO}$ , and  $\text{TiO}_2$ , are also screened to tailor desired grain orientation (Chen et al., 2017; Leng et al., 2014; Li et al., 2018b; Wen et al., 2017). In these window layers,  $n$ -type  $\text{CdS}$  is widely used in the commercial CIGS and  $\text{CdTe}$  solar cells because its optical bandgap of  $\sim 2.4$  eV allows the sunlight to pass through it with relatively low absorption (Oladeji et al., 2000). However, not only the  $\text{CdTe}$ , but also the  $\text{Sb}_2\text{Se}_3$  cells with  $\text{CdS}$  window layers still suffer from the low photocurrent (i.e., short circuit current,  $J_{\text{sc}}$ , loss) due to the absorption loss of blue light with a bandgap of  $> 2.4$  eV (Paudel and Yan, 2014). The experimental value of the short circuit current,  $J_{\text{sc}}$ , of  $\text{Sb}_2\text{Se}_3$  devices with  $\text{CdS}$  window layer has been reported to be above  $28.4 \text{ mA cm}^{-2}$  for the  $\text{FTO}/\text{CdS}/\text{Sb}_2\text{Se}_3$  superstrate structure, and the  $32.58 \text{ mA cm}^{-2}$  for the  $\text{Mo}/\text{MoSe}_2/\text{Sb}_2\text{Se}_3/\text{CdS}$  substrate device structure, respectively (Li et al., 2018a; Li et al., 2019). But, the experimental photocurrent is still far from the theoretical one ( $\sim 42 \text{ mA cm}^{-2}$ ) (Lin et al., 2018). In addition, the  $\text{CdS}/\text{Sb}_2\text{Se}_3$  device also experienced severe degradation, and the fundamental cause is still not well-understood (Chen et al., 2017; Wang et al., 2017a).

It has been demonstrated that the  $\text{CdSe}$  is a better window layer with higher photocurrent than that of the conventional  $\text{CdS}$  (bandgap  $\sim 2.4$  eV) window layer in  $\text{CdTe}$  solar cells although  $\text{CdSe}$  should absorb more light at short wavelength ( $< 550$  nm) due to its 1.7 eV bandgap and thus reduce the photocurrent (Baines et al., 2018). It is reported that the improved photocurrent in  $\text{CdSe}/\text{CdTe}$  device is originated from the formation of gradient bandgap in the  $\text{CdSeTe}$  absorber induced by  $\text{CdSe}/\text{CdTe}$  interdiffusion to form a graded ternary  $\text{CdSeTe}$  absorber with a minimum bandgap 1.34 eV due to  $\text{CdSe}-\text{CdTe}$  bowing behavior (Poplawsky et al., 2016). In other words, the interdiffusion between  $\text{CdSe}$  and  $\text{CdTe}$  absorber could fully consume the  $\text{CdSe}$  and form a “window-free” like  $\text{FTO}/\text{CdSeTe}/\text{CdTe}$  devices with graded absorbers allowing more short wavelength light absorbed. The consumption of  $\text{CdSe}$  window layer not only benefits the light absorption at short wavelength but also enhances the photocurrent at long wavelength (e.g., reduced bandgap in grading absorber will enhance the light absorption at long wavelength) (Paudel and Yan, 2014; Poplawsky et al., 2016). Thus, to further improve the photocurrent of  $\text{Sb}_2\text{Se}_3$  solar cells,  $\text{CdSe}$  window layer requires further investigation.

In this work, we prepare  $\text{Sb}_2\text{Se}_3$  thin films with sputtered  $\text{CdSe}$  window layer using CSS on  $\text{FTO}$ -coated glass substrates. We demonstrate that the  $\text{CdSe}$  window layer could suppress the  $\text{Se}$  interdiffusion at the interfacial area in the  $\text{CdSe}/\text{Sb}_2\text{Se}_3$  device, and significantly improve the device stability. It is shown that the degradation in the  $\text{CdS}/\text{Sb}_2\text{Se}_3$  is dominated by the  $\text{S}/\text{Se}$  interdiffusion between the  $\text{CdS}$  and  $\text{Sb}_2\text{Se}_3$  layer. Meanwhile,  $\text{CdSe}$  can also improve the photocurrent of the  $\text{CdSe}/\text{Sb}_2\text{Se}_3$  device. With the optimized growth condition in CSS, the champion PCE with the architecture of  $\text{glass}/\text{FTO}/\text{CdSe}/\text{Sb}_2\text{Se}_3/\text{graphite}/\text{Ag}$  can reach 4.5%. The mechanism of the improved stability and photocurrent by  $\text{CdSe}$  window layer was analyzed using both experimental data and one-dimensional (1D) device simulation. Our findings in the present work further confirm the enormous potential of  $\text{Sb}_2\text{Se}_3$  as an emerging low-cost, scalable thin-film PV for affordable solar energy.

## 2. Experimental section

### 2.1. Solar cell fabrication

About 80 nm thick  $\text{CdSe}$  window layers were deposited on a cleaned commercial 3.2 mm fluorine doped  $\text{SnO}_2$  coated soda-lime glass ( $\text{FTO}$  TEC15, Pilkington, US) by sputtering as described previously (Paudel et al., 2015). The  $\text{FTO}$  substrate was cleaned using the acetone, isopropanol, and deionized water in an ultrasonic bath for 30 min, respectively and dried in  $\text{N}_2$  gas flow.  $\text{CdSe}$  window layers were magnetron sputtered on the cleaned  $\text{FTO}$  substrate with a 50 W RF power at

250 °C substrate temperature and in an ambient of 10 mTorr Ar pressure (Paudel et al., 2015; Paudel and Yan, 2014). For comparison, the 80 nm thick  $\text{CdS}$  window layer was deposited using chemical bath deposition (CBD) as reported elsewhere (Contreras et al., 2002).  $\text{Sb}_2\text{Se}_3$  thin films with thicknesses of  $\sim 900$  nm were grown in vacuum using a commercial CSS system (MTI, US). The high purity  $\text{Sb}_2\text{Se}_3$  powder (99.999%, Alfa Aesar, US) was placed on the bottom AlN plate, and the  $\text{CdSe}$  coated  $\text{FTO}$  substrate was loaded on the top AlN plate (5 mm distance from the  $\text{Sb}_2\text{Se}_3$  powder). To optimize the growth conditions of  $\text{Sb}_2\text{Se}_3$  absorber on both  $\text{CdS}$  and  $\text{CdSe}$  window layers, the substrate and sources temperatures were tuned from 250–350 °C, and 500–580 °C, respectively at chamber pressure about 5 mTorr (Guo et al., 2018). Here, we used the optimal CSS conditions for both window layers, i.e., 300 °C for substrate and 550 °C for source during the  $\text{Sb}_2\text{Se}_3$  CSS deposition to rule out the impact of  $\text{Sb}_2\text{Se}_3$  CSS deposition conditions on the device performance. The as-grown  $\text{Sb}_2\text{Se}_3$  films were cleaned with a deionized water rinse and dried using the  $\text{N}_2$  flow, and graphite and Ag paste was then screen-printed on  $\text{Sb}_2\text{Se}_3$  (with an active area of  $0.08 \text{ cm}^2$ ).

### 2.2. Materials characterization

The film microstructure was characterized by X-ray diffraction (XRD) System (Philips X'Pert). The film morphologies and chemical composition were characterized by the scanning electron microscope (SEM, JEOL 7000) and electron-dispersive spectroscopy (EDS) attached to the SEM. The Raman experiments were conducted on a single stage Raman spectrometer with a solid-state laser (Horiba LabRam HR, 532 nm wavelength). The absorbance and transmittance spectra were measured using a UV–Vis spectrometer (Shimadzu UV-1800). The surface mor were recorded using atomic force microscopy (AFM, Park XE70). The film thickness was measured by the surface profilometer (KLA Tenor D-500) and validated through the SEM cross-sectional image. The secondary ion mass spectrometry (SIMS, IMS-4f, CAMECA Instrument) was employed to characterize the quantitative compositional depth profile using 5.5 keV  $\text{O}_2^+$  beam with an analyzed area of  $250 \times 250 \mu\text{m}^2$ .

### 2.3. Solar cell measurement and simulation

The current–voltage ( $J$ - $V$ ) curve of the cells were characterized using a solar simulator (Newport, Oriel Class AAA 94063A, 1000 Watt Xenon light source) with a source meter (Keithley 2420) at  $100 \text{ mW/cm}^2$  AM 1.5G irradiation. A calibrated Si-reference cell and meter (Newport, 91150 V, certificated by NREL) was used to calibrate the solar simulator before each measurement. External quantum efficiency (EQE) data were performed by a solar cell spectral response measurement system (QE-T, Enli Technology, Co. Ltd). The solar cell device simulation was performed using the solar cell capacitance simulator (SCAPS) simulation for both  $\text{CdS}$  and  $\text{CdSe}$  in an  $\text{FTO}/\text{window layer}/\text{Sb}_2\text{Se}_3/\text{graphite}$  architecture (detailed simulation parameters can be found in the Table S1 and S2) (Burgelman et al., 2000).

## 3. Results and discussion

Fig. 1a shows the X-ray diffraction (XRD) spectra of the as-grown CBD deposited  $\text{CdS}$  and sputtered  $\text{CdSe}$  on the  $\text{FTO}$  glass substrate. The film deposition conditions were reported previously (Hu et al., 2018b; Paudel and Yan, 2014). Both  $\text{CdS}$  and  $\text{CdSe}$  films (thickness  $\sim 60$  nm) are cubic-phase with zinc blende structure although the peaks from the window layer overlap with the peaks from the  $\text{FTO}$  substrate (Guo et al., 2018; Kim et al., 2016). To ascertain the phase structure, Raman spectra were collected for both window layers, as shown in Fig. 1b. The results of Raman spectra provide more details on the structure of  $\text{CdS}$  and  $\text{CdSe}$  films, especially the fundamental first-order longitudinal (1LO) optical phonon mode at  $\sim 300 \text{ cm}^{-1}$  for  $\text{CdS}$  and  $\sim 203 \text{ cm}^{-1}$  for

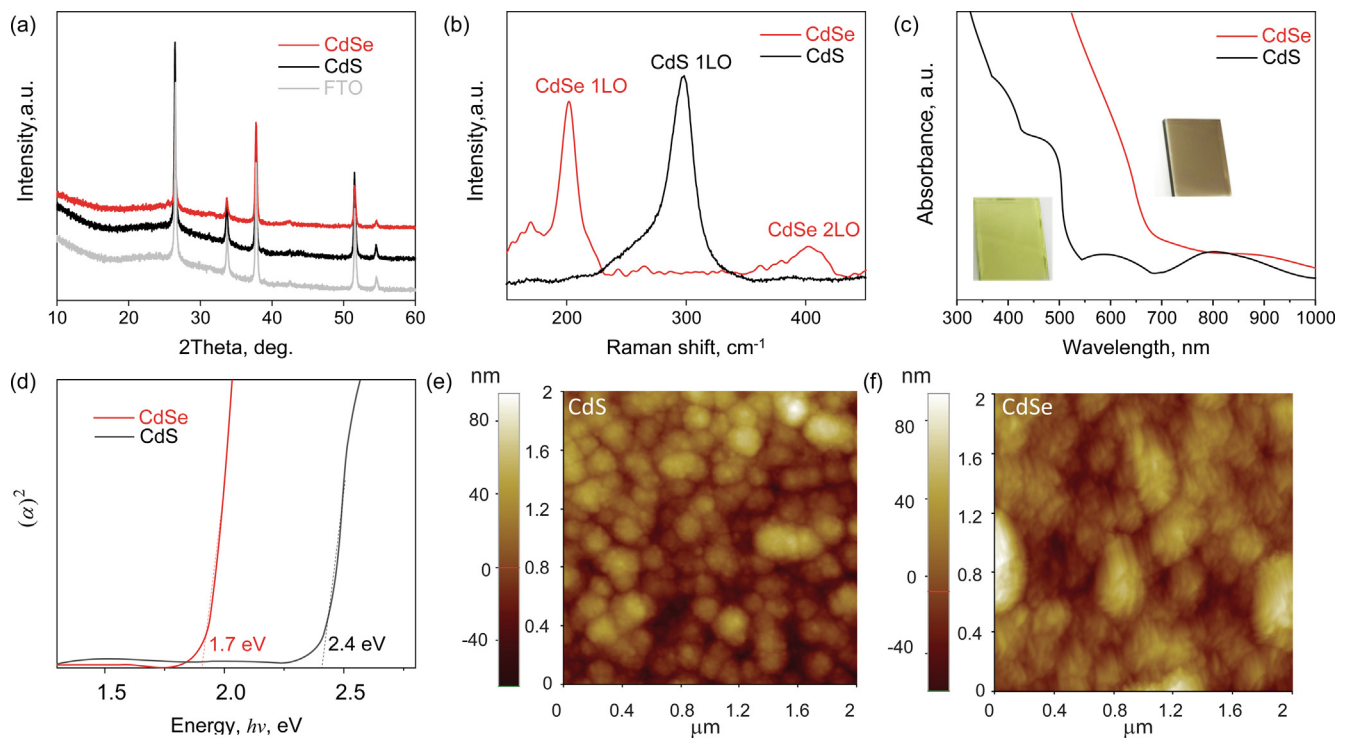


**Fig. 1.** Phase structure, optical property and surface morphology of the CdSe and CdS window layer. (a) X-ray diffraction spectra, (b) Raman spectra, (c) optical absorption, (d) bandgap, and (e) and (f) AFM topography.

CdSe, respectively (Kevin et al., 2015; Trajic et al., 2015). The 1LO Raman lines are broad which slightly shift toward the lower frequency compared with their bulk counterparts ( $210\text{ cm}^{-1}$  for bulk CdSe and  $305\text{ cm}^{-1}$  for bulk CdS) due to the small dispersion of the LO mode phonon wave vectors in polycrystalline films (Oladeji et al., 2000). The slightly redshift by several wavenumbers that the particle size of both window layers is at nanoscale due to phonon confinement effect (Trajic et al., 2015). However, the phonon confinement effect of the nanoscale grain size may not impact the window layer absorption (e.g., bandgap) because of the uniform dispersion of grains (Dzhagan et al., 2008). Fig. 1c shows the optical absorption for CdS and CdSe window layer measured using ultraviolet–visible spectroscopy (UV–Vis). The images of the window layers are shown in the inset of Fig. 1c. The CdSe is dark brown while CdS is slightly yellow, in agreement with the optical absorption edges at 520 nm and 730 nm for CdS and CdSe, respectively. Fig. 1d shows that the fit of the bandgap plot determines the optical bandgap of CdS and CdSe at 2.4 and 1.7 eV, respectively. The morphology of the window layers is characterized by the atomic force microscopy (AFM), as shown in Fig. 1e–f for CdS and CdSe, respectively. The CdS layer shows the root-mean-square (RMS) roughness of  $\sim 0.66\text{ nm}$ , and the CdSe layer is rougher with RMS roughness of  $\sim 3.14\text{ nm}$ . The CdSe grain size is larger than that of the CdS grain size, potentially due to the higher substrate temperature during sputtering deposition at  $250^\circ\text{C}$ . The rough surface, large grain size and slightly larger lattice parameters of cubic CdSe film may impact the following  $\text{Sb}_2\text{Se}_3$  film texture, window/absorber interface, and even the solar cell device performance which will be discussed later. However, the sputtered CdSe buffer layer deposition conditions for  $\text{Sb}_2\text{Se}_3$  should be further optimized to reduce its surface roughness.

The  $\text{Sb}_2\text{Se}_3$  films on both CdSe and CdS window layer were grown by the CSS technique. The growth conditions were optimized by varying the substrate and source temperature. The CSS growth parameters for both CdS and CdSe window layers are set to  $300^\circ\text{C}$  for the substrate temperature and  $550^\circ\text{C}$  for the source temperature. The XRD spectra for the as-grown  $\text{Sb}_2\text{Se}_3$  films are shown in Fig. 2a, which shows an orthorhombic structure (JCPDS 15-0861). (Hu et al., 2018b) Both

films show strongly preferred (2 2 1)-orientation, while the undesired (1 2 0)-orientation peaks are very weak, suggesting the good quality of the CSS-grown  $\text{Sb}_2\text{Se}_3$  films (Zhou et al., 2015). To compare the impact of the CdSe and CdS window layer on the crystalline behavior of  $\text{Sb}_2\text{Se}_3$ , the texture coefficients (TCs) of three representative peaks, i.e. (1 2 0) peak ( $2\theta \sim 16.9^\circ$ ), (2 1 1) peak ( $2\theta \sim 28.2^\circ$ ), and (2 2 1) peak ( $2\theta \sim 31.1^\circ$ ), are calculated using the measured XRD spectra, as shown in Fig. 2b. Through the TC equation,  $TC_{hkl} = \frac{I_{(hkl)}}{I_{0(hkl)}} / (\frac{1}{N} \sum_{i=1}^N \frac{I_{(h_k l_i)}}{I_{0(h_k l_i)}})$ , where  $I_{(hkl)}$  is the diffraction peak intensity of  $(h\ k\ l)$  plane, and  $I_{0(hkl)}$  is the diffraction peak intensity of  $(h\ k\ l)$  plane in the standard XRD pattern, i.e., JCPDS 15-0861, the TCs of (1 2 0), (2 1 1) and (2 2 1) peaks were determined. The TC value of less than 1 means no texture behavior (e.g., TC of (1 2 0) plane), while the TC value of larger than 1 means enhanced textured orientation in this direction (e.g., TCs of (2 1 1) and (2 2 1)). The texture coefficient also suggests that the  $\text{Sb}_2\text{Se}_3$  film with CdSe window layer has a slightly lower TC than that of the CdS window layer in (2 2 1) and (2 1 1), which could be due to the smoother CdS surface, as shown in Fig. 1e and f. The larger grain size and rougher surface of CdSe buffer layer can disturb the  $(\text{Sb}_4\text{Se}_6)_n$  ribbon growth normal to the substrate during the CSS deposition due to the rougher interface between CdSe and  $\text{Sb}_2\text{Se}_3$ . Fig. 2c and d show the top-view and cross-sectional SEM images of the  $\text{Sb}_2\text{Se}_3$  film with CdS and CdSe window layer, respectively. The film thickness is about  $1\ \mu\text{m}$  in both window layers. The grain size of both films is around  $300\text{ nm}$ . The  $\text{Sb}_2\text{Se}_3$  film with CdS window layer shows some strip-like grains on the surface, which was observed in CSS deposited  $\text{Sb}_2\text{Se}_3$  film at a higher substrate temperature ( $\sim 330^\circ\text{C}$ ) with strong (1 2 0) XRD peak (Li et al., 2018a). The potential reason for these strip-like grains on the surface may be due to extra vapor residing on the surface during the cooling process which may affect back-contact collection and impact the device performance (Wang et al., 2017a). The EDS spectra detected on both film surfaces show that the atomic ratio between Se and Sb was close to 3:2 (59.5:40.5 for CdS/ $\text{Sb}_2\text{Se}_3$  and 60.1:39.9 for CdSe/ $\text{Sb}_2\text{Se}_3$ ) as shown in Fig. S2 (see the supporting information), thus both are close to the stoichiometric composition.



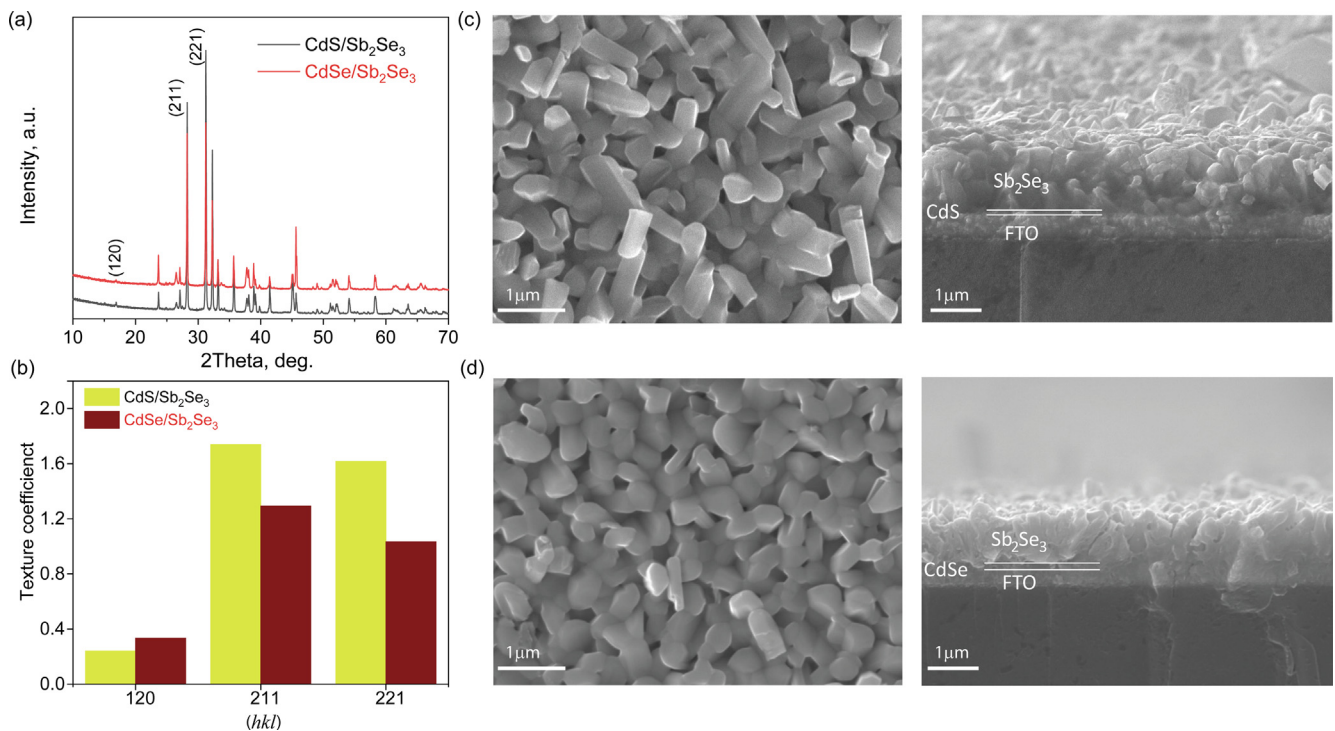


**Fig. 2.** Crystal structure of the CSS-grown Sb<sub>2</sub>Se<sub>3</sub> films with CdS and CdSe window layers. (a) XRD spectra of the Sb<sub>2</sub>Se<sub>3</sub>, (b) texture coefficient, (c) and (d) top view and cross-sectional SEM images for CdS and CdSe window layer, respectively.

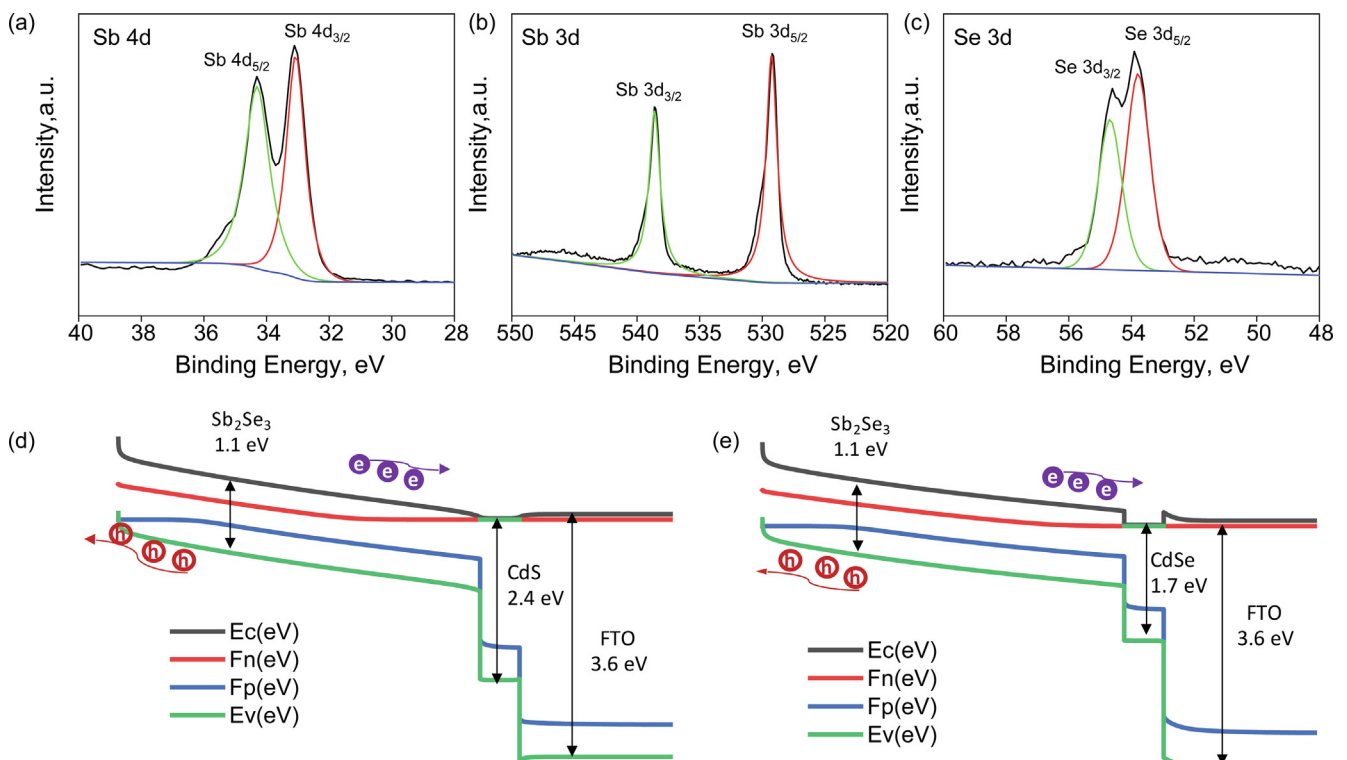


**Fig. 3.** XPS analysis for (a) Sb 4d, (b) Se 3d and (c) Sb 3d, and calculated bandgap alignment (d) CdS and (e) CdSe of the Sb<sub>2</sub>Se<sub>3</sub> film with CdSe window layer.

X-ray photoelectron spectroscopy (XPS) measurement was performed for both CdS/Sb<sub>2</sub>Se<sub>3</sub> and CdSe/Sb<sub>2</sub>Se<sub>3</sub> films. As the two films show similar XPS results, only the results of CdSe/Sb<sub>2</sub>Se<sub>3</sub> film are shown in Fig. 3 to help identify the oxidation state of Sb and Se. The XPS spectra were calibrated using the C 1s peak at 284.6 eV. Fig. 3a shows the Sb 4d high-resolution XPS spectrum with the binding energy

at 34.2 eV and 33.0 eV for Sb 4d<sub>3/2</sub> and Sb 4d<sub>5/2</sub>, respectively, which exclude the presence of Sb<sup>5+</sup>. Fig. 3b shows the Sb 3d high-resolution XPS spectrum with the binding energy at 538.1 eV and 529.0 eV for Sb 3d<sub>3/2</sub> and Sb 3d<sub>5/2</sub>, respectively, suggesting no Sb<sub>2</sub>O<sub>3</sub> formed on the surface (Liu et al., 2014; Wang et al., 2017b). Fig. 3c shows the Se 3d spectrum with binding energy at 54.1 eV and 55.0 eV for Se 3d<sub>5/2</sub> and

Se 3d<sub>3/2</sub>, indicating no clear elemental Se residual on the surface. Thus, the strip-like grains of the CdS buffered Sb<sub>2</sub>Se<sub>3</sub> in Fig. 2c could not be associated with the extra residing vapor during the cooling process and may originate from the buffer layer morphology induced growth (Kondrotas et al., 2019).

Prior to the device fabrication, we performed device simulation for Sb<sub>2</sub>Se<sub>3</sub> thin film solar cells with CdS and CdSe window layers using the Solar Cells Capacitance Simulator (SCAPS) to understand the operation mechanism (see the details of the device simulation method in supporting information). The bandgap of Sb<sub>2</sub>Se<sub>3</sub> (~1.1 eV) was characterized using the UV–Vis absorption (Guo et al., 2018). The simulated energy bandgap diagrams under illumination for these two window layers are shown in Fig. 3d and e for CdS and CdSe, respectively, suggesting a type II band alignment are formed at the interface of CdSe (CdS)/Sb<sub>2</sub>Se<sub>3</sub>. Both the conduction-band edge ( $E_c$ ) and valence-band edge ( $E_v$ ) of Sb<sub>2</sub>Se<sub>3</sub> is higher than that of CdSe and CdS window layer, i.e.  $E_c(\text{Sb}_2\text{Se}_3) > E_c(\text{CdSe(S)})$  and  $E_v(\text{Sb}_2\text{Se}_3) > E_v(\text{CdSe(S)})$ . The interface valence band offset for CdS window layer ( $\Delta E_{V, \text{CdS/Sb}_2\text{Se}_3} \sim 1.55$  eV) is larger than that of the CdSe ( $\Delta E_{V, \text{CdSe/Sb}_2\text{Se}_3} \sim 1.2$  eV) window layer. While the interface conduction band offset for the CdS window layer ( $\Delta E_{C, \text{CdS/Sb}_2\text{Se}_3} \sim 0.2$  eV) is less than that of the CdSe window layer ( $\Delta E_{C, \text{CdSe/Sb}_2\text{Se}_3} \sim 0.4$  eV) due to the higher electron affinity and smaller bandgap of CdSe. Here, both the conduction and valence band positions of CdS are better than CdSe, indicating that the CdS window layer is more desired for the Sb<sub>2</sub>Se<sub>3</sub> solar cells. However, the following device performance measurement indicates that the CdSe/Sb<sub>2</sub>Se<sub>3</sub> solar cells show higher photocurrent at short wavelength than that of the CdS/Sb<sub>2</sub>Se<sub>3</sub>, which is similar to the CdSe/CdTe compared with CdS/CdTe.

Fig. 4a and b show the measured current–voltage ( $J$ - $V$ ) curves and external quantum efficiency (EQE) of the Sb<sub>2</sub>Se<sub>3</sub> cells with CdS and CdSe window layers under illumination, respectively. The device performance of 65 devices (Fig. 4c) shows an average efficiency of 3.9% for CdS and 4.3% for CdSe window layers, respectively. The champion device performance, including  $V_{oc}$ ,  $J_{sc}$ , and fill factor ( $FF$ ) and PCE, are shown in Table 1. The  $J$ - $V$  curves indicate that the cell with an 80 nm CdS window layer has a slightly higher  $V_{oc}$  (i.e., 0.377 V in CdS vs. 0.354 V in CdSe window layer) and a lower  $J_{sc}$  than that of the cells with CdSe window layer (i.e., 25.68 mA cm<sup>-2</sup> in CdS vs. 27.57 mA cm<sup>-2</sup> in CdSe). Here, the relative low  $V_{oc}$  is similar to other CSS deposited Sb<sub>2</sub>Se<sub>3</sub> without hole transport layer (Li et al., 2018a). A similar  $J_{sc}$  improvement was observed in CdTe thin film solar cells with CdSe window layer when CdSe was fully consumed by the CdTe film during CdTe deposition and CdCl<sub>2</sub> treatment (e.g., consumption up to 350 nm CdSe by 4  $\mu$ m CdTe) (Paudel and Yan, 2014). Here, we propose that similar behavior occurs at the CdSe/Sb<sub>2</sub>Se<sub>3</sub> interface. Considering the CdSe-Sb<sub>2</sub>Se<sub>3</sub> pseudo-binary phase diagram (see the details in the supporting information, Fig. S1), the only single ternary compound is CdSb<sub>2</sub>Se<sub>4</sub>. The solubility of CdSe in Sb<sub>2</sub>Se<sub>3</sub> at 450 °C is about 6 mol. %

**Table 1**

Device performance parameters of champion Sb<sub>2</sub>Se<sub>3</sub> cells with CdS and CdSe window layers.

Window layer	$V_{oc}$ , V	$J_{sc}$ , mA cm <sup>-2</sup>	$FF$ , %	$R_{oc}$ , $\Omega$ cm <sup>2</sup>	$R_{sh}$ , $\Omega$ cm <sup>2</sup>	PCE, %
CdS	0.377	25.68	43.00	88.93	983.20	4.16
CdSe	0.354	27.57	46.13	60.90	903.09	4.51

and the solubility of Sb<sub>2</sub>Se<sub>3</sub> in CdSe at 450 °C is 1.5 mol.%. Here, the interdiffusion between the 80 nm CdSe and 1  $\mu$ m Sb<sub>2</sub>Se<sub>3</sub> during deposition (i.e., 300 °C) is highly possible although the solubility will be slightly less than 6 mol.% at low substrate temperature (Vasyly Tomashyk and Shcherbak, 2013). Therefore, the 80 nm CdSe may be consumed by the 1  $\mu$ m Sb<sub>2</sub>Se<sub>3</sub> and form the Cd-Sb-Se ternary compounds at the FTO/CdSe/Sb<sub>2</sub>Se<sub>3</sub> interfaces. The PCE of the CdSe/Sb<sub>2</sub>Se<sub>3</sub> cell can reach as high as 4.5% with a graphite back contact without further optimization using the hole transport layer (HTL), while the CdS/Sb<sub>2</sub>Se<sub>3</sub> cells achieve PCE of 4.16%. The PCE statistical analysis of the Sb<sub>2</sub>Se<sub>3</sub> cells with CdS and CdSe window layer is shown in Fig. 4c. The improved efficiency mainly comes from the improved current and higher fill factor compared with the CdS/Sb<sub>2</sub>Se<sub>3</sub> cells.

The measured EQE curves (Fig. 4b) provide more details about the improved device performance, for the enhanced  $J_{sc}$  of CdSe window layer cells. The Sb<sub>2</sub>Se<sub>3</sub> cell with CdS window layer shows a current loss for the blue photons (i.e., short wavelength) due to the higher bandgap of CdS (2.4 eV). Meanwhile, the Sb<sub>2</sub>Se<sub>3</sub> cell with CdSe window layer shows clear photocurrent gain at the blue region, and a slight redshift (~8 nm from 998 nm to 1006 nm corresponding to ~0.01 eV redshift of cells with CdS window layer) was observed. As a comparison, a Sb<sub>2</sub>Se<sub>3</sub> cell without a window layer (i.e., FTO/Sb<sub>2</sub>Se<sub>3</sub>) was fabricated as a reference. The results are shown in Fig. 4b, and the window free cell shows a significant current loss as the photoexcited hole and electron cannot be efficiently collected. Using the CdSe window layer, the Sb<sub>2</sub>Se<sub>3</sub> cell with a ~80 nm CdSe window layer gains about 1.89 mA cm<sup>-2</sup> more current than the cell with CdS window layer. The improved current collection mainly originates from the blue light regions, as shown in supporting information Fig. S3a. Regarding the experimental EQE, the weak response between 500 and 1100 nm can be attributed to the high series resistance and reflections in each layer and junction.

It is known that the CdS buffered Sb<sub>2</sub>Se<sub>3</sub> devices show quick degradation under illumination, (Wang et al., 2017a; Zhou et al., 2015) which is associated with the interfacial diffusion between CdS and Sb<sub>2</sub>Se<sub>3</sub>. (Zhou et al., 2017) This kind of interdiffusion also exists in the conventional CdS/CdTe, CdSe/CdTe, and CdS/CuInGaSe heterostructure solar cells, and generates the degradation issues (Mathew et al., 2012; Poplawsky et al., 2016; Salomé et al., 2017). However, previous reports consider Cd diffusion as the dominant degradation mechanism of CdS/Sb<sub>2</sub>Se<sub>3</sub> device performance (Wang et al., 2017a).

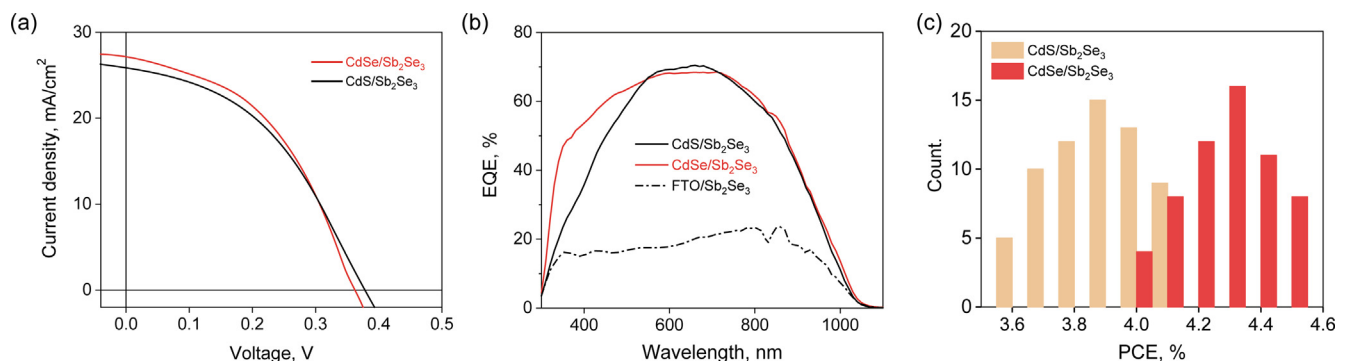


**Fig. 4.** Device performance of the Sb<sub>2</sub>Se<sub>3</sub> cells with CdS and CdSe window layers. (a) the current density–voltage ( $J$ - $V$  curve), (b) experimental EQE spectra, and (c) histogram of PCE for CdS and CdSe window layers.

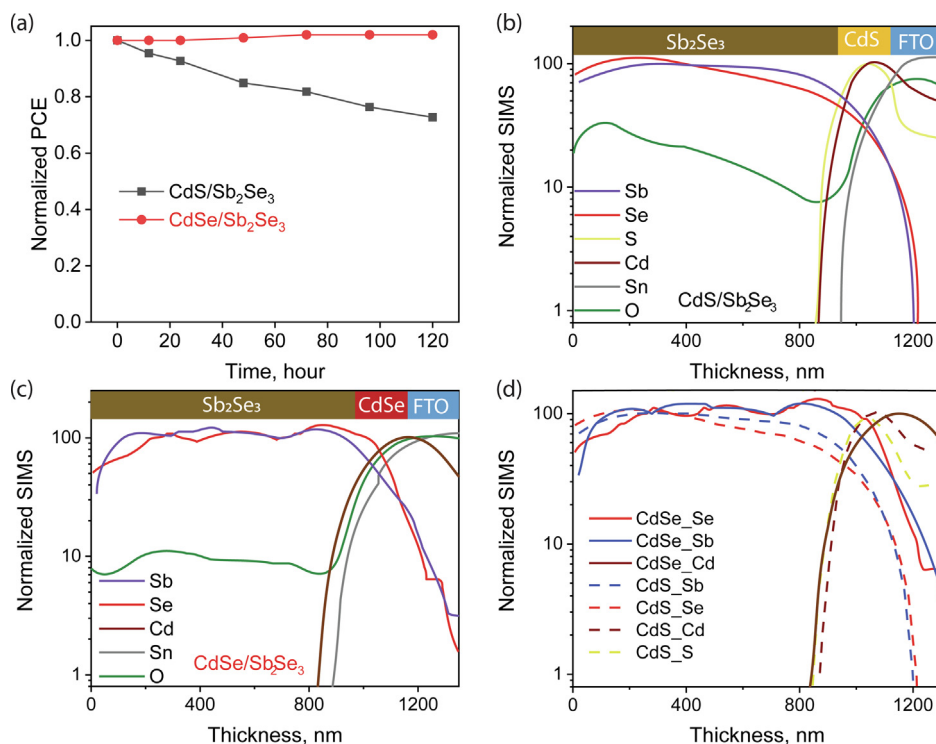


**Fig. 5.** (a) Light soak stability test (85 °C, 1sun solar simulator). (b) and (c) Secondary ion mass spectroscopy (SIMS) depth profile of the CdS and CdSe buffered Sb<sub>2</sub>Se<sub>3</sub> thin film. (d) Comparison of Se, Sb, Cd in (b) and (c) SIMS profile.

Here, we test both CdS/Sb<sub>2</sub>Se<sub>3</sub> and CdSe/Sb<sub>2</sub>Se<sub>3</sub> device stability under light soaking at 85 °C and 1 Sun (100 mW cm<sup>-2</sup>) using a Metal Halide Lamp, as shown in Fig. 5a. For the CdS/Sb<sub>2</sub>Se<sub>3</sub> device, the PCE degraded up to 70% of its initial efficiency after about 120 h, which is much faster than that of CdS/Sb<sub>2</sub>Se<sub>3</sub> devices light soaking at 50 °C, 1.3sun (82% degradation in 1300 h) as reported previously (Chen et al., 2017). Surprisingly, the CdSe/Sb<sub>2</sub>Se<sub>3</sub> device is more stable than that of CdS/Sb<sub>2</sub>Se<sub>3</sub> device, and no degradation was found at 120 h at 85 °C, and 1 Sun light-soaking condition, similar to that of ZnO or Al<sub>2</sub>O<sub>3</sub> buffered Sb<sub>2</sub>Se<sub>3</sub> (Wang et al., 2017a). This suggests that the CdSe layer could remarkably improve device stability. The chemical concentration gradient between CdSe and Sb<sub>2</sub>Se<sub>3</sub> is limited to Cd and Sb interdiffusion (*i.e.*, finite Se concentration gradient). However, with these Cd/Sb interdiffusion, the degradation did not occur in CdSe/Sb<sub>2</sub>Se<sub>3</sub> device, suggesting that Cd diffusion may not dominate the degradation of the Sb<sub>2</sub>Se<sub>3</sub> device since both CdS and CdSe have Cd. The Cd diffusion could cause Cd to occupy the Sb position and reduce the *p*-type conduction of Sb<sub>2</sub>Se<sub>3</sub>, which may benefit the device performance due to the reduced interfacial defects (Wang et al., 2017a; Zhou et al., 2017). However, in the CdS/Sb<sub>2</sub>Se<sub>3</sub> device with severe degradation, S diffuses into Sb<sub>2</sub>Se<sub>3</sub> driven by the S concentration gradient at the CdS/Sb<sub>2</sub>Se<sub>3</sub> interface. Thus, S diffusion should dominate the degradation behavior of the CdS/Sb<sub>2</sub>Se<sub>3</sub> devices.

To ascertain the root cause of the degradation mechanism in CdS/Sb<sub>2</sub>Se<sub>3</sub> and reveal the interdiffusion at the interface between the window layers (*i.e.* CdS vs. CdSe) and the absorber Sb<sub>2</sub>Se<sub>3</sub> layer, secondary ion mass spectrometry (SIMS) was employed to explore the in-depth analysis of Cd, S, Se and Sb diffusion behavior. Fig. 5b and c show the normalized SIMS depth profiling for CdS and CdSe window layer, respectively. To compare the difference between these two window layers, they are plotted together in Fig. 5d. The Cd diffusion level is identical as expected because of the same window layer thickness and the same Sb<sub>2</sub>Se<sub>3</sub> deposition conditions for both CdS and CdSe window layer. Thus, we can minimize the impact of Cd on the stability of the CdS/Sb<sub>2</sub>Se<sub>3</sub> device. As for the Se diffusion profile, CdSe/Sb<sub>2</sub>Se<sub>3</sub> device has much higher Se concentration at the interfacial area than that of

CdS/Sb<sub>2</sub>Se<sub>3</sub>. However, the Se concentration at the CdS/Sb<sub>2</sub>Se<sub>3</sub> interface has been significantly reduced, and the S ions diffuse into the Sb<sub>2</sub>Se<sub>3</sub> about 100 nm. These Se and S interdiffusion at the interface of CdS/Sb<sub>2</sub>Se<sub>3</sub> can produce interfacial defects (*e.g.*, Se<sub>s</sub> and S<sub>se</sub>) and lead to the degradation, while the CdSe/Sb<sub>2</sub>Se<sub>3</sub> is ultra-stable during light soaking due to the smoother and simpler interfacial atmosphere.

#### 4. Conclusions

In summary, we have demonstrated that the degradation mechanism in the CdS/Sb<sub>2</sub>Se<sub>3</sub> is dominated by the S diffusion from CdS to the Sb<sub>2</sub>Se<sub>3</sub>. Utilizing CdSe window layer could stabilize the device performance during light soaking. The improved photocurrent in Sb<sub>2</sub>Se<sub>3</sub> cells with CdSe window layer was originated from the enhanced light absorption from the blue spectrum of the visible light. The CdSe/Sb<sub>2</sub>Se<sub>3</sub> thin film solar cells with 4.5% PCE can be achieved in glass/FTO/CdSe/Sb<sub>2</sub>Se<sub>3</sub>/graphite architecture grown by close space sublimation. The improved photocurrent, *J*<sub>sc</sub>, by employing CdSe window layer could be associated with an enhanced conduction band offset and thus improved electron transport at the CdSe/Sb<sub>2</sub>Se<sub>3</sub> heterojunction. The observed results demonstrate that CdSe could be integrated into Sb<sub>2</sub>Se<sub>3</sub> solar cells to suppress degradation and improve the photocurrent. Our results also suggest that Sb<sub>2</sub>Se<sub>3</sub> device performance can be further improved by interfacial engineering.

#### Acknowledgements

L.P.G. and F.Y. acknowledge the support from the resources of Alabama Water Institute at The University of Alabama, and the National Science Foundation under Grant No. 1844210. B.Z. and X.Q. acknowledge the support from Texas A&M University.

#### Appendix A. Supplementary data

Supplementary data to this article can be found online at <https://doi.org/10.1016/j.solener.2019.06.042>.



## References

- Baines, T., Zoppi, G., Bowen, L., Shalvey, T.P., Mariotti, S., Durose, K., Major, J.D., 2018. Incorporation of CdSe layers into CdTe thin film solar cells. *Sol. Energy Mater. Sol. Cells* 180, 196–204.
- Bosio, A., Rosa, G., Romeo, N., 2018. Past, present and future of the thin film CdTe/CdS solar cells. *Sol. Energy* 175, 31–43.
- Burgelman, M., Nollet, P., Degraeve, S., 2000. Modelling polycrystalline semiconductor solar cells. *Thin Solid Films* 361, 527–532.
- Chen, C., Li, K., Chen, S., Wang, L., Lu, S., Liu, Y., Li, D., Song, H., Tang, J., 2018. Efficiency improvement of  $\text{Sb}_2\text{Se}_3$  solar cell via grain boundary inversion. *ACS Eng. Lett.* 3, 2335–2341.
- Chen, C., Zhao, Y., Lu, S., Li, K., Li, Y., Yang, B., Chen, W., Wang, L., Li, D., Deng, H., 2017. Accelerated optimization of  $\text{TiO}_2/\text{Sb}_2\text{Se}_3$  thin film solar cells by high-throughput combinatorial approach. *Adv. Eng. Mater.* 7, 1700866.
- Contreras, M.A., Romero, M.J., To, B., Hasoon, F., Noufi, R., Ward, S., Ramanathan, K., 2002. Optimization of CBD CdS process in high-efficiency  $\text{Cu}(\text{In}, \text{Ga})\text{Se}_2$ -based solar cells. *Thin Solid Films* 403–404, 211.
- Deng, H., Yuan, S., Yang, X., Zhang, J., Khan, J., Zhao, Y., Ishaq, M., Ye, W., Cheng, Y.-B., Song, H., Tang, J., 2018. High-throughput method to deposit continuous composition spread  $\text{Sb}_2(\text{Se}, \text{S}_{1-x})_3$  thin film for photovoltaic application. *Prog. Photovolt. Res. Appl.* 26 (4), 281–290.
- Dzhagan, V.M., Ya Valakh, M., Raevskaya, A.E., Stroyuk, A.L., Kuchmiy, S.Y., Zahn, D.R.T., 2008. Size effects on Raman spectra of small CdSe nanoparticles in polymer films. *Nanotech.* 19 (30), 305707.
- Green, M.A., Bremner, S.P., 2016. Energy conversion approaches and materials for high-efficiency photovoltaics. *Nat. Mater.* 16, 23.
- Guo, L., Zhang, B., Qin, Y., Li, D., Li, L., Qian, X., Yan, F., 2018. Tunable quasi-one-dimensional ribbon enhanced light absorption in  $\text{Sb}_2\text{Se}_3$  thin-film solar cells grown by close-space sublimation. *Sol. RRL* 2, 1800128.
- Hu, X., Tao, J., Chen, S., Xue, J., Weng, G., Kaijiang, Hu, Z., Jiang, J., Chen, S., Zhu, Z., Chu, J., 2018a. Improving the efficiency of  $\text{Sb}_2\text{Se}_3$  thin-film solar cells by post-annealing treatment in vacuum condition. *Sol. Energy Mater. Sol. Cells* 187, 170–175.
- Hu, X., Tao, J., Weng, G., Jiang, J., Chen, S., Zhu, Z., Chu, J., 2018b. Investigation of electrically-active defects in  $\text{Sb}_2\text{Se}_3$  thin-film solar cells with up to 5.91% efficiency via admittance spectroscopy. *Sol. Energy Mater. Sol. Cells* 186, 324–329.
- Hutter, O.S., Phillips, L.J., Durose, K., Major, J.D., 2018. 6.6% efficient antimony selenide solar cells using grain structure control and an organic contact layer. *Sol. Energy Mater. Sol. Cells* 188, 177–181.
- Kevin, P., Alghamdi, Y.G., Lewis, D.J., Azad Malik, M., 2015. Morphology and band gap controlled AACVD of CdSe and  $\text{CdS}_x\text{Se}_{1-x}$  thin films using novel single source precursors: Bis(diethylthio/diselenocarbamate)cadmium(II). *Mat. Sci. Semicon. Proc.* 40, 848–854.
- Khan, M.D., Aamir, M., Sohail, M., Sher, M., Akhtar, J., Malik, M.A., Revaprasadu, N., 2018. Novel single source precursor for synthesis of  $\text{Sb}_2\text{Se}_3$  nanorods and deposition of thin films by AACVD: photo-electrochemical study for water reduction catalysis. *Sol. Energy* 169, 526–534.
- Kim, D., Jang, Y.-J., Jung, H.-S., Kim, M., Baek, D., Yi, J., Lee, J., Choi, Y., 2016. Optimization of CdS buffer layer for high efficiency CIGS solar cells. *J. Nanosci. Nanotechnol.* 16, 5074–5077.
- Kondrotas, R., Zhang, J., Wang, C., Tang, J., 2019. Growth mechanism of  $\text{Sb}_2\text{Se}_3$  thin films for photovoltaic application by vapor transport deposition. *Sol. Energy Mater. Sol. Cells* 199, 16–23.
- Leng, M., Luo, M., Chen, C., Qin, S., Chen, J., Zhong, J., Tang, J., 2014. Selenization of  $\text{Sb}_2\text{Se}_3$  absorber layer: an efficient step to improve device performance of  $\text{CdS}/\text{Sb}_2\text{Se}_3$  solar cells. *Appl. Phys. Lett.* 105 (8), 083905.
- Li, D.-B., Yin, X., Grice, C.R., Guan, L., Song, Z., Wang, C., Chen, C., Li, K., Cimaroli, A.J., Awni, R.A., 2018a. Stable and efficient  $\text{CdS}/\text{Sb}_2\text{Se}_3$  solar cells prepared by scalable close space sublimation. *Nano. Eng.* 49, 346–353.
- Li, K., Kondrotas, R., Chen, C., Lu, S., Wen, X., Li, D., Luo, J., Zhao, Y., Tang, J., 2018b. Improved efficiency by insertion of  $\text{Zn}_{1-x}\text{Mg}_x\text{O}$  through sol-gel method in  $\text{ZnO}/\text{Sb}_2\text{Se}_3$  solar cell. *Sol. Energy* 167, 10–17.
- Li, Z., Liang, X., Li, G., Liu, H., Zhang, H., Guo, J., Chen, J., Shen, K., San, X., Yu, W., Schropp, R.E.I., Mai, Y., 2019. 9.2%-efficient core-shell structured antimony selenide nanorod array solar cells. *Nat. Commun.* 10 (1), 125.
- Liang, G.-X., Zheng, Z.-H., Fan, P., Luo, J.-T., Hu, J.-G., Zhang, X.-H., Ma, H.-L., Fan, B., Luo, Z.-K., Zhang, D.-P., 2018. Thermally induced structural evolution and performance of  $\text{Sb}_2\text{Se}_3$  films and nanorods prepared by an easy sputtering method. *Sol. Energy Mater. Sol. Cells* 174, 263–270.
- Lin, L.-Y., Jiang, L.-Q., Qiu, Y., Fan, B.-D., 2018. Analysis of  $\text{Sb}_2\text{Se}_3/\text{CdS}$  based photovoltaic cell: a numerical simulation approach. *J. Phys. Chem. Solids* 122, 19–24.
- Liu, X., Chen, C., Wang, L., Zhong, J., Luo, M., Chen, J., Xue, D.-J., Li, D., Zhou, Y., Tang, J., 2015. Improving the performance of  $\text{Sb}_2\text{Se}_3$  thin film solar cells over 4% by controlled addition of oxygen during film deposition. *Prog. Photovolt. Res. Appl.* 23 (12), 1828–1836.
- Liu, X., Chen, J., Luo, M., Leng, M., Xia, Z., Zhou, Y., Qin, S., Xue, D.-J., Lv, L., Huang, H., Niu, D., Tang, J., 2014. Thermal evaporation and characterization of  $\text{Sb}_2\text{Se}_3$  thin film for substrate  $\text{Sb}_2\text{Se}_3/\text{CdS}$  solar cells. *ACS Appl. Mater. Inter.* 6 (13), 10687–10695.
- Liu, X., Xiao, X., Yang, Y., Xue, D.-J., Li, D.-B., Chen, C., Lu, S., Gao, L., He, Y., Beard, M.C., Wang, G., Chen, S., Tang, J., 2017. Enhanced  $\text{Sb}_2\text{Se}_3$  solar cell performance through theory-guided defect control. *Prog. Photovolt. Res. Appl.* 25 (10), 861–870.
- Mathew, X., Cruz, J.S., Coronado, D.R., Millán, A.R., Segura, G.C., Morales, E.R., Martínez, O.S., Garcia, C.C., Landa, E.P., 2012. CdS thin film post-annealing and Te-S interdiffusion in a CdTe/CdS solar cell. *Sol. Energy* 86 (4), 1023–1028.
- Ngo, T.T., Chavhan, S., Kosta, I., Miguel, O., Grande, H.-J., Tena-Zaera, R., 2014. Electrodeposition of antimony selenide thin films and application in semiconductor sensitized solar cells. *ACS Appl. Mater. Inter.* 6 (4), 2836–2841.
- Oladeji, I.O., Chow, L., Liu, J.R., Chu, W.K., Bustamante, A.N.P., Fredricksen, C., Schulte, A.F., 2000. Comparative study of CdS thin films deposited by single, continuous, and multiple dip chemical processes. *Thin Solid Films* 359 (2), 154–159.
- Paudel, N.R., Poplawsky, J.D., Moore, K.L., Yan, Y., 2015. Current enhancement of CdTe-based solar cells. *IEEE J. Photovolt.* 5 (5), 1492–1496.
- Paudel, N.R., Yan, Y., 2014. Enhancing the photo-currents of CdTe thin-film solar cells in both short and long wavelength regions. *Appl. Phys. Lett.* 105 (18), 183510.
- Polman, A., Knight, M., Garnett, E.C., Ehrler, B., Sinke, W.C., 2016. Photovoltaic materials: present efficiencies and future challenges. *Science* 352 (6283).
- Poplawsky, J.D., Guo, W., Paudel, N., Ng, A., More, K., Leonard, D., Yan, Y., 2016. Structural and compositional dependence of the  $\text{CdTeSe}_{1-x}$  alloy layer photoactivity in CdTe-based solar cells. *Nat. Commun.* 7, 12537.
- Rajagopal, A., Yao, K., Jen, A.K.Y., 2018. Toward perovskite solar cell commercialization: a perspective and research roadmap based on interfacial engineering. *Adv. Mater.* 30 (32), 1800455.
- Razykov, T.M., Shukurov, A.X., Atabayev, O.K., Kuchkarov, K.M., Ergashev, B., Mavlonov, A.A., 2018. Growth and characterization of  $\text{Sb}_2\text{Se}_3$  thin films for solar cells. *Sol. Energy* 173, 225–228.
- Salomé, P.M.P., Ribeiro-Andrade, R., Teixeira, J.P., Keller, J., Törndahl, T., Nicoara, N., Edoff, M., González, J.C., Leitão, J.P., Sadewasser, S., 2017. Cd and Cu interdiffusion in  $\text{Cu}(\text{In}, \text{Ga})\text{Se}_2/\text{CdS}$  hetero-interfaces. *IEEE J. Photovolt.* 7 (3), 858–863.
- Shongalova, A., Correia, M.R., Teixeira, J.P., Leitão, J.P., González, J.C., Ranjbar, S., Garud, S., Vermang, B., Cunha, J.M.V., Salomé, P.M.P., Fernandes, P.A., 2018. Growth of  $\text{Sb}_2\text{Se}_3$  thin films by selenization of RF sputtered binary precursors. *Sol. Energy Mater. Sol. Cells* 187, 219–226.
- Sivaram, V., Kann, S., 2016. Solar power needs a more ambitious cost target. *Nat. Energy* 1, 16036.
- Steinmann, V., Brandt, R.E., Buonassisi, T., 2015. Non-cubic solar cell materials. *Nat. Photonics* 9, 355.
- Trajic, J., Gilic, M., Romcevic, N., Romcevic, M., Stanišić, G., Hadzic, B., Petrovic, M., Yahia, Y.S., 2015. Raman spectroscopy of optical properties in Cds thin films 47, 145–152.
- Vasyl Tomashyk, P.F., Shcherbak, Larysa, 2013. Ternary Alloys Based on II-VI Semiconductor Compounds. CRC Press.
- Wang, L., Li, D.-B., Li, K., Chen, C., Deng, H.-X., Gao, L., Zhao, Y., Jiang, F., Li, L., Huang, F., He, Y., Song, H., Niu, G., Tang, J., 2017a. Stable 6%-efficient  $\text{Sb}_2\text{Se}_3$  solar cells with a ZnO buffer layer. *Nat. Energy* 2, 17046.
- Wang, L., Li, D.-B., Li, K., Chen, C., Deng, H.-X., Gao, L., Zhao, Y., Jiang, F., Li, L., Huang, F., He, Y., Song, H., Niu, G., Tang, J., 2017b. Stable 6%-efficient  $\text{Sb}_2\text{Se}_3$  solar cells with a ZnO buffer layer. *Nature Energy* 2 (4).
- Wang, X., Tang, R., Yin, Y., Ju, H., Li, S.a., Zhu, C., Chen, T., 2019. Interfacial engineering for high efficiency solution processed  $\text{Sb}_2\text{Se}_3$  solar cells. *Sol. Energy Mater. Sol. Cells* 189, 5–10.
- Wen, X., He, Y., Chen, C., Liu, X., Yang, B., Leng, M., Song, H., Zeng, K., Li, D., Li, K., 2017. Magnetron sputtered ZnO buffer layer for  $\text{Sb}_2\text{Se}_3$  thin film solar cells. *Sol. Energy Mater. Sol. Cells* 172, 74–81.
- Yuan, C., Zhang, L., Liu, W., Zhu, C., 2016. Rapid thermal process to fabricate  $\text{Sb}_2\text{Se}_3$  thin film for solar cell application. *Sol. Energy* 137, 256–260.
- Zhang, L., Jiang, C., Wu, C., Ju, H., Jiang, G., Liu, W., Zhu, C., Chen, T., 2018.  $\text{V}_2\text{O}_5$  as hole transporting material for efficient all inorganic  $\text{Sb}_2\text{S}_3$  solar cells. *ACS Appl. Mater. Inter.* 10 (32), 27098–27105.
- Zhao, B., Wan, Z., Luo, J., Jia, C., Liu, X., Wang, R., 2018. Improving the performance of  $\text{Sb}_2\text{Se}_3$  sensitized solar cells with a versatile CdSe layer modification. *Appl. Mater. Today* 12, 191–197.
- Zhou, Y., Li, Y., Luo, J., Li, D., Liu, X., Chen, C., Song, H., Ma, J., Xue, D.-J., Yang, B., Tang, J., 2017. Buried homojunction in  $\text{CdS}/\text{Sb}_2\text{Se}_3$  thin film photovoltaics generated by interfacial diffusion. *Appl. Phys. Lett.* 111 (1), 013901.
- Zhou, Y., Wang, L., Chen, S., Qin, S., Liu, X., Chen, J., Xue, D.-J., Luo, M., Cao, Y., Cheng, Y., Sargent, E.H., Tang, J., 2015. Thin-film  $\text{Sb}_2\text{Se}_3$  photovoltaics with oriented one-dimensional ribbons and benign grain boundaries. *Nat. Photon.* 9, 409.